

APPLICATIONS OF ION IMPLANTATION FOR MODIFICATION OF TiO₂: A REVIEW

A.L. Stepanov

Laser Zentrum Hannover, 30419 Hannover, Germany

Kazan Federal University, 420018 Kazan, Russian Federation

Kazan Physical-Technical Institute, Russian Academy of Sciences, 420029 Kazan, Russian Federation

Received: December 29, 2011

Abstract. Ion implantation can be successfully used for modification physical-chemical properties of TiO₂. A review of applications for implanted TiO₂ is presented and demonstrated perspectives in the fields such as magnetic data storage, nano-catalysts and optics. Solid solutions with implanted magnetic ions demonstrated anisotropic ferromagnetism at room temperature. Nanoparticles synthesized in titanium dioxide by implantation with noble metal ions give possibilities to fabricate plasmonic and optical composites. Different parameters and condition of ion implantation technology and realized specific properties of irradiated titanium dioxide observed and discussed.

1. INTRODUCTION

The search for new functional materials is one of the defining characteristics of modern science and technology. Novel mechanical, electrical, magnetic, chemical, biological, and optical devices are often the result of the fabrication of new materials. A significant amount of research on TiO₂ was performed over the last decades and a number of reviews on various aspects of TiO₂ were published, for example [1-3]. To enhance the quality of TiO₂, many producing methods were proposed to dope (or incorporate) trace impurity into TiO₂ including: ion-assisted sputtering, chemical vapor deposition, sol-gel, chemical mixing, magnetron sputtering, and ion implantation. A comprehensive list of doping methods of TiO₂ is presented in a review [3]. Most of the promising technology for modification and improvement of TiO₂ properties is ion implantation [4-8] because it allows reaching a high impurity filling factor in an irradiated matrix beyond the equilibrium limit of impurity solubility and, in the same time, provides controllable synthesis of metal or

semiconductor nanoparticles (NPs) at various depths under the substrate surface. This method allows for strict control of the doping ion beam position on the sample surface with implant dose as, for example, in the case of electron- and ion-beam lithography. Today, ion implantation is well developed and widely used in industrial semiconductor chip and optical waveguides fabrication. Therefore, for instance, the combination of ion-doped TiO₂ with semiconductor or dielectric substrates by same technique as ion implantation could be reached quite effective in practice. Several approaches for TiO₂ modification was recently proposed: metal-ion implantation of TiO₂ (using transition metals such as Cu, Co, Ni, Cr, Mn, Mo, Nb, V, Fe, Ru, Au, Ag, Pt) [9-11], reduced TiO_x photocatalysts [12, 13], non-metal doped-TiO₂ (for example, N, S, C, B, P, I, F) [14-16] and so on. In the present review, recent advantages and some examples on application of ion implantation for modification of TiO₂ are discussed in the frame of novel photocatalytic, electric, optical and magnetic properties of doped TiO₂.

Corresponding author: A.L. Stepanov, e-mail: aanstep@gmail.com

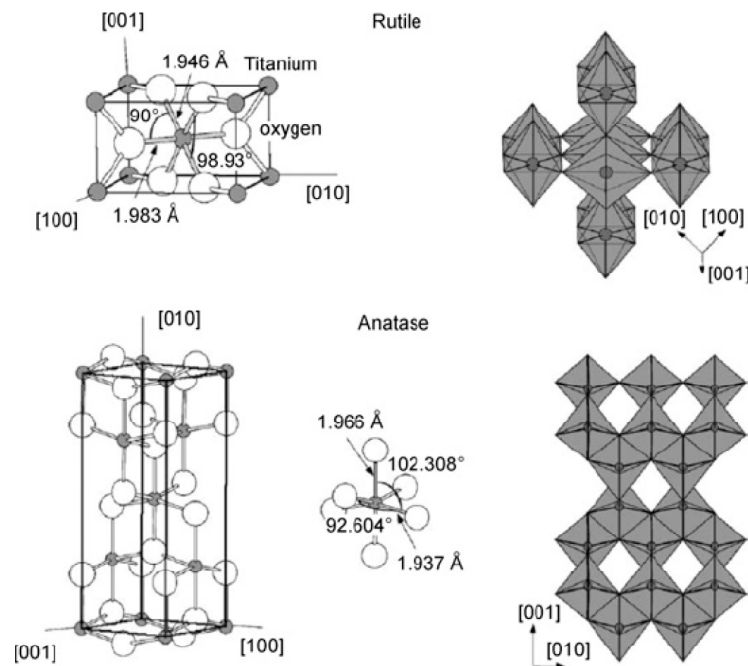


Fig. 1. Crystal structures of the rutile and anatase phases of TiO_2 . Fragment of an image from Ref. [25].

2. PHYSICAL AND CHEMICAL PROPERTIES OF TiO_2

2.1. Structures

TiO_2 belongs to the family of transition metal oxides. Short description of chemical structure of TiO_2 was done in the review [1]. There are four commonly known polymorphs of TiO_2 found in nature: anatase (tetragonal), brookite (orthorhombic), rutile (tetragonal), and TiO_2 (B) (monoclinic) [17-20]. Besides these polymorphs, two additional high-pressure forms have been synthesized from the rutile phase. These are TiO_2 (II) [21] with a PbO_2 structure and TiO_2 (H) [22] with a hollandite structure.

Rutile: Rutile TiO_2 has a tetragonal structure and contains 6 atoms per unit cell (Fig. 1). The TiO_6 octahedron is slightly distorted [23-25]. The rutile phase is stable at most temperatures and pressures up to 60 kbar, where TiO_2 (II) becomes the thermodynamically favorable phase [26]. It was found that anatase and brookite structures transformed to the rutile phase after reaching a certain nanoparticle size, with the rutile phase becoming more stable than anatase for particle sizes greater than 14 nm [27]. Once the rutile phase formed, it grew much faster than the anatase. The activity of the rutile phase as a photocatalyst is generally very poor. However, it was suggested that the rutile phase can be active or inactive, depending on its preparation conditions [28].

Anatase: Anatase TiO_2 also has a tetragonal structure but the distortion of the TiO_6 octahedron is slightly larger for the anatase phase [20,24], as depicted in Fig. 1. It was found that the anatase phase is more stable than the rutile at 0K, but the energy difference between these two phases is small (2 to 10 kJ/mol) [29]. The increased photoreactivity is because of the slightly higher Fermi level, lower capacity to adsorb oxygen and higher degree of hydroxylation in the anatase phase [30]. It was reported that the reactivity of (001) facets is greater than that of (101) facets in an anatase crystal [31]. In the work [32] it was synthesized uniform anatase crystals containing 47% (001) facets using hydrofluoric acid as a morphology-controlling agent.

Brookite: Brookite TiO_2 belongs to the orthorhombic crystal system. Its unit cell is composed of 8 formula units of TiO_2 and is formed

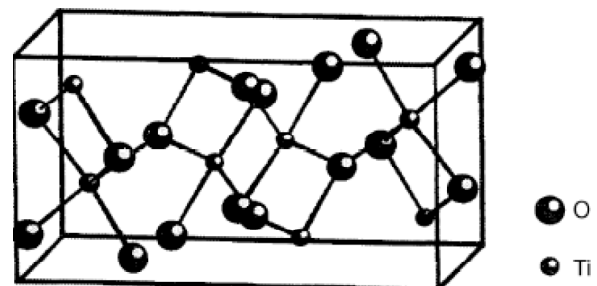


Fig. 2. Lattice structure of brookite TiO_2 . Fragment of an image from Ref. [24].

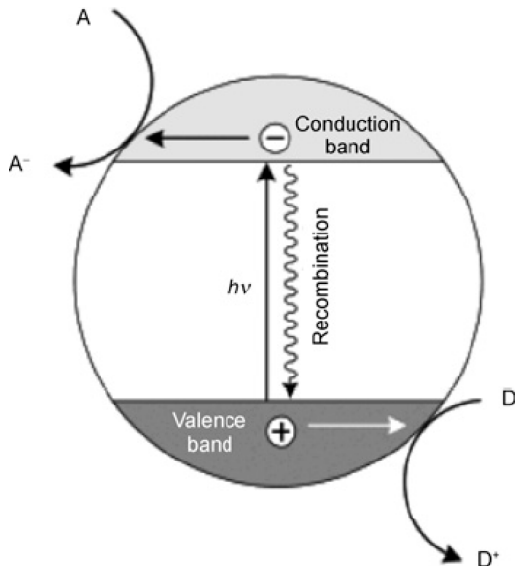


Fig. 3. Mechanism of light absorption by TiO_2 . Fragment of an image from Ref. [33].

by edge-sharing TiO_6 octahedra (Fig. 2). It is more complicated, has a larger cell volume and is also the least dense of the 3 forms and is not often used for experimental investigations [24].

TiO_2 is a large band semiconductor, with band gaps of 3.2, 3.02, and 2.96 eV for the anatase, rutile and brookite phases, respectively [33]. The valence band of TiO_2 is composed of the 2p orbitals of oxygen hybridized with the 3d orbitals of titanium, while the conduction band is only the 3d orbitals of titanium [34].

2.2. Photoactivity

When TiO_2 is exposed to near-UV light, electrons in the valence band are excited to the conduction band leaving behind holes (h^+), as shown in Fig. 3. The excited electrons (e^-) in the conduction band are now in a purely 3d state and because of dissimilar parity, the transition probability of e^- to

the valence band decreases, leading to a reduction in the probability of e^-/h^+ recombination [35].

Anatase TiO_2 is considered to be the active photocatalytic component based on charge carrier dynamics, chemical properties and the activity of photocatalytic degradation of organic compounds. It has inherent surface band bending that forms spontaneously in a deeper region with a steeper potential compared with the rutile phase (Fig. 4) [36] thus surface hole trapping dominates because spatial charge separation is achieved by the transfer of photogenerated holes towards the surface of the particle via the strong upward band bending. However, in the rutile phase, the bulk recombination of electrons and holes occurs, so only holes very close to the surface are trapped and transferred to the surface.

As was reviewed in the work [2] TiO_2 represents an effective photocatalyst for water and air purification and for self-cleaning surfaces. Additionally, it can be used as antibacterial agent because of strong oxidation activity and superhydrophilicity. TiO_2 shows relatively high reactivity and chemical stability under ultraviolet light ($\lambda < 387\text{nm}$). The development of photocatalysts exhibiting high reactivity under visible light ($\lambda > 400\text{nm}$) should allow the main part of the solar spectrum, even under poor illumination of interior lighting, to be used.

The photocatalytic mechanism is initiated by the absorption of the photon $h\nu_1$ with energy equal to or greater than the band gap of TiO_2 ($\sim 3.2\text{eV}$ for the anatase phase) producing an electron-hole pair on the surface of TiO_2 as schematized in Fig. 5. An electron is promoted to the conduction band (CB) while a positive hole is formed in the valence band (VB). Excited-state electrons and holes can recombine and dissipate the input energy as heat, get trapped in metastable surface states, or react with electron donors and electron acceptors

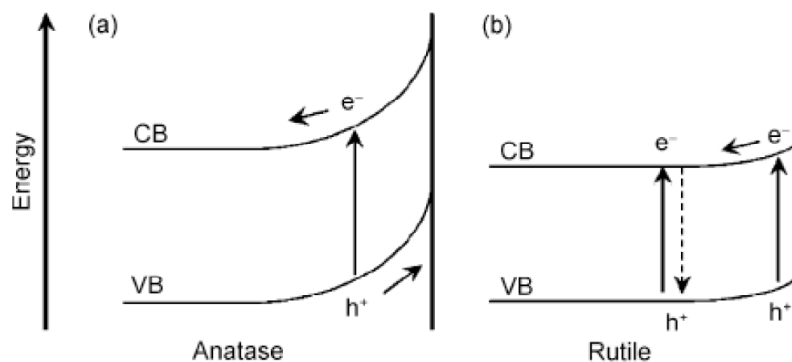


Fig. 4. Surface band bending of the anatase (a) and rutile phases of TiO_2 (b). Fragment of an image from Ref. [36].

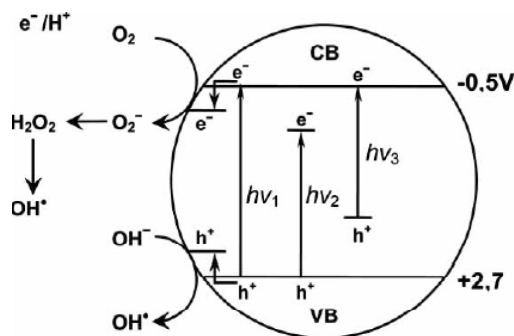


Fig. 5. Mechanism of TiO_2 photocatalysis: $h\nu_1$: pure TiO_2 ; $h\nu_2$: metal-doped TiO_2 and $h\nu_3$: nonmetal-doped TiO_2 . Fragment of an image from Ref. [2].

adsorbed on the semiconductor surface or within the surrounding electrical double layer of the TiO_2 . After reaction with water, these holes can produce hydroxyl radicals with high redox oxidizing potential [2]. Depending upon the exact conditions, the holes, OH radicals, O_2^- , H_2O_2 , and O_2 itself can play important roles in the photocatalytic reaction mechanism [37, 38].

The visible light photoactivity of metal-doped TiO_2 can be explained by a new energy level produced in the band gap of TiO_2 in the TiO_2 matrix. As shown in Fig. 5, electron can be excited from the defect state to the TiO_2 conduction band by photon with energy equals $h\nu_2$. Additional benefit of metal doping is the improved trapping of electrons to inhibit electron-hole recombination during irradiation. Decrease of charge carriers recombination results in enhanced photoactivity.

There are three different main opinions regarding modification mechanism of TiO_2 doped with nonmetals [2]. (1) Band gap narrowing; (2) Impurity energy levels; and (3) Oxygen vacancies. (1). *Band gap narrowing*: it was found that N $2p$ state hybrids with O $2p$ states in anatase TiO_2 doped with nitrogen because their energies are very close, and thus the band gap of N: TiO_2 is narrowed and able to absorb visible light [39]. (2). *Impurity energy level*: it was stated that TiO_2 oxygen sites substituted by nitrogen atom form isolated impurity energy levels above the valence band [40]. Irradiation with UV light excites electrons in both the VB and the impurity energy levels, but illumination with visible light only excites electrons in the impurity energy level. (3). *Oxygen vacancies*: it was concluded that oxygen-deficient sites formed in the grain boundaries are important to emerge vis-activity and nitrogen doped in part of oxygen-deficient sites are important as a blocker for reoxidation [41].

The modification mechanism of anatase doped with nonmetals was also analyzed in the work [42]. It was studied N: TiO_2 and concluded that TiO_2 doped with substitutional nitrogen has shallow acceptor states above the valence state. In contrast, TiO_2 doped with interstitial nitrogen has isolated impurity states in the middle of the band gap. These impurity energy levels are mainly hybridized by N $2p$ states and O $2p$ states.

3. ION IMPLANTATION

3.1. General principles

Ion implantation is an effective technological tool for introducing single impurities into the surface layer of the substrate to a depth of several micrometers. The degree of surface modification of the materials depends on their individual chemical and structural properties, as well as on variations of implantation parameters, such as the type and energy of an implant, current density in ion beam, substrate temperature, etc. A most critical parameter is ion dose F_0 , which determines the implant amount. Depending on the modification of materials, such as TiO_2 , by irradiation, ion implantation can be conventionally divided into low-dose and high-dose processes.

In the case of a low-dose irradiation ($\sim F_0 \leq 5.0 \cdot 10^{14}$ ion/cm²), the ions implanted after stopping and thermalization are dispersed throughout the volume of the materials and are well separated from each other. The energy of the implant is transferred to the matrix via electron shell excitation (ionization) and nuclear collisions. This causes radiation-induced defects, which, in turn, may reversibly or irreversibly modify the material structure [4]. Various types of crystal structure damage have been observed in practice: extended and point defects, amorphization and local crystallization, precipitation of a new phase made up of host atoms or implanted ions, etc.

The range of high-dose implantation may be divided into two characteristic dose sub-ranges. In the range $10^{15} \leq \sim F_0 \leq 10^{17}$ ion/cm², the concentration of metal and semiconductor ions exceeds the solubility limit of metal atoms in matrices and the system relaxes by nucleation and growth of NPs as illustrated cross-section view (Fig. 6) [8, 43]. The threshold dose value (at which NPs nucleate) depends on the type of the dielectric matrix and implant. For example, for 25-keV Ag^+ -ion implantation into LiNbO_3 , the threshold dose was found to be $F_0 \sim 5.0 \cdot 10^{15}$ ion/cm² [44], for 30-keV silver ions embedded in epoxy resin, $F_0 \sim 10^{16}$

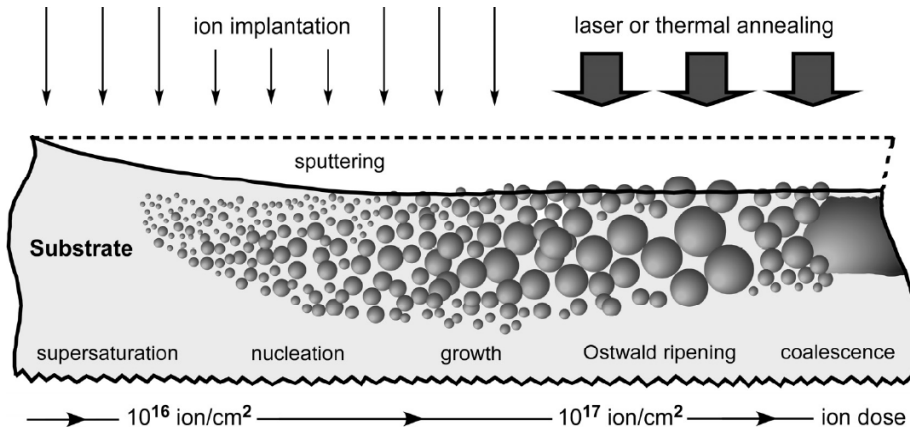


Fig. 6. Basic physical processes (from left to right) involved in the formation of nanoparticle from an implant vs. the ion dose with regard to surface sputtering under irradiation [8].

ion/cm² [45]. The next sub-range of high-dose implantation, $\sim F_0 \leq 10^{17}$ ion/cm², leads to the coalescence of already existing NPs with the formation of either NP aggregates or thin quasi-continuous films at the dielectric surface. For instance, the irradiation of silicone polymer-glass by 30-keV Ag ions at higher-than threshold-nucleation doses favors the formation of aggregate structures [43]. The MNP distribution established in the dielectrics after coalescence or Ostwald ripening may be dramatically disturbed by post-implantation thermal or laser annealing [46].

3.2. Depth distributions of implanted transition metal ions in TiO₂

Implantation at low and medium energies (10–300 keV) is of particular interest for this purpose, since it results in ultrathin composite layers. One of the important and challenging experimental implantation problems is to determine the geometrical parameters of the depth profiles of the impurity concentration in a target. With such data, every one can find the implantation dose range characteristic of the formation of NPs in an implanted layer, the modified-layer thickness, and the limiting implanted impurity concentration to be reached under given implantation conditions.

Since all these parameters are important, the problem can be considered via computer simulation of the deceleration of accelerated ions in a target. However, the literature-available data tables of calculated depth profile parameters, which are mainly composed for the ion implantation of single-component materials (Si, Ge, Cu, etc.), and software like TRIM (Transport of Ions in Matter) or SRIM (Stopping and Range of Ions in Solids) [47] give a

good result for low dose ion implantation only (Fig. 7) but they cannot be applied for medium and high ion implantation doses ($>10^{15}$ ions/cm²), since they do not take into account the sputtering of the surface and the irradiation-induced change in the elemental composition of the implanted layer. The depth profiles calculated by these computer programs and based on the Monte Carlo statistical distribution differ substantially from the real experimental depth profiles of medium-energy ions.

The problem of surface sputtering can be solved via the simulation of depth profiles with the DYNA (Dynamic Numerical Analysis) software package [48–50], which is based on the effects of pair collisions of implanted ions with substrate atoms. These

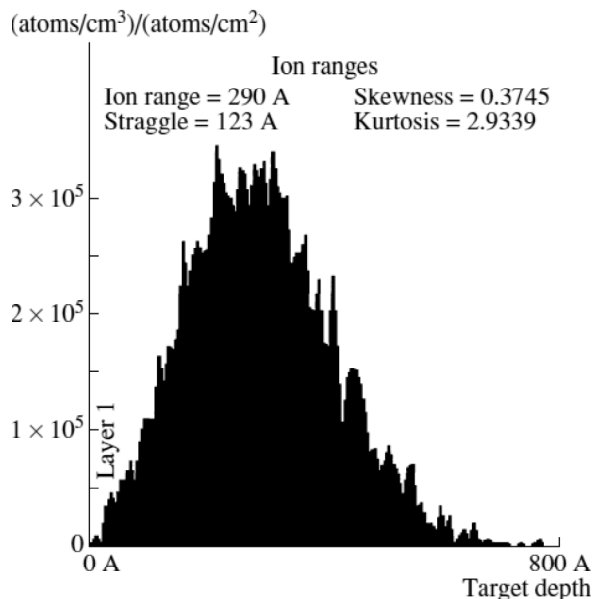


Fig. 7. Depth profile of cobalt ions implanted into TiO₂ that was calculated by the SRIM software package [52].

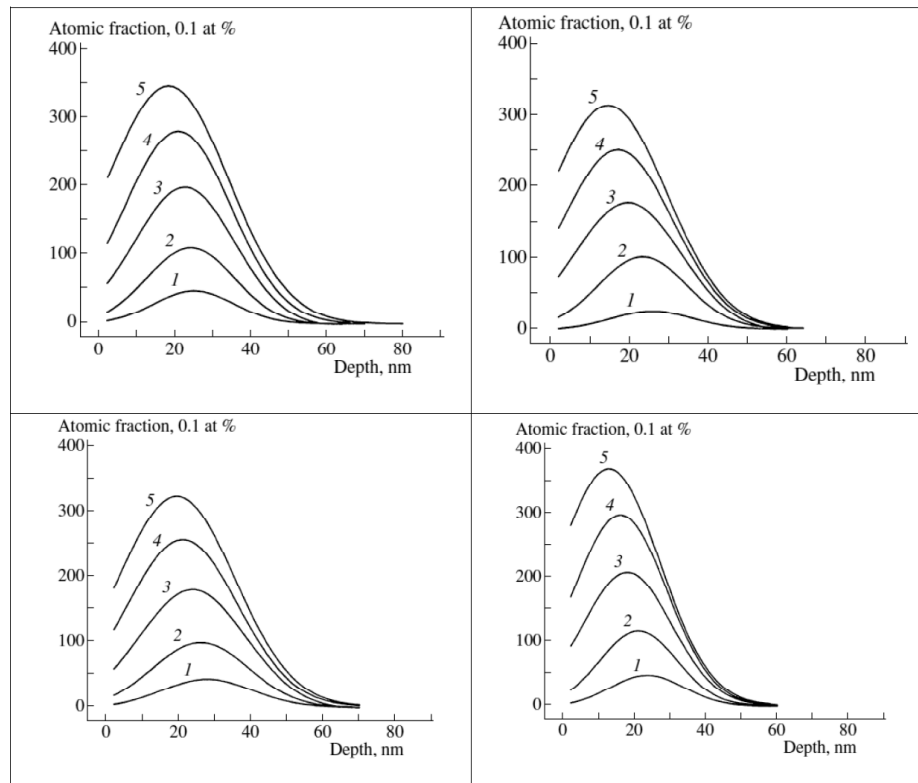


Fig. 8. Depth profiles of 40-keV Co⁺ (top left), Co⁺ (with surface sputtering, top right), Cr⁺ (bottom, left) and Cu⁺ (bottom, right) ions implanted into a TiO_2 matrix that were calculated at a dose of (1) 10^{16} , (2) $2.5 \cdot 10^{16}$, (3) $5 \cdot 10^{16}$, (4) $7.5 \cdot 10^{16}$, and (5) 10^{17} ions/cm² without surface sputtering [52].

effects can take into account a dynamic change in the elemental composition of the near-surface layer in the implanted substrate and its surface sputtering. The elastic scattering of a moving accelerated ion by target atoms is described in this software package using the results of theoretical work [48]. The DYNA program has already reached good agreement between the calculated and experimental depth profiles of impurities for the simple cases of implantation of high-energy (>300 keV) relatively light ions only in monoatomic metallic and semiconductor substrates [48,49]. Moreover, depth profiles were successfully analyzed for heavy ions (Cu^+ , Ag^+ , Au^+) implanted in polyatomic insulators (SiO_2 , Al_2O_3 , soda-lime silica glass) at various irradiation energies (30, 60, 100 keV) [51].

Therefore, as it was demonstrated [52] the DYNA algorithm calculation procedure for the case of implantation of transition metal ions, such as chromium, cobalt, and copper, into a polyatomic TiO_2 matrix can be successfully applied. To describe the dynamic change in the elemental composition of the near-surface layer in the implanted material during cascade pair collisions and atomic mixing, we have to determine the volumes of the atoms

involved in these processes. These volumes were calculated from the density data of the corresponding solids or, e.g., for the oxygen atom, from the interatomic distances in the insulators under study. Using the SRIM-2006 software [47], it was estimated [52] the sputtering coefficients of insulator substrates that are required for DYNA calculations for the normal incidence of implanted ions depending on their energy with allowance for the surface energy and the binding energy between atoms in titanium dioxide. For example, the sputtering coefficient of TiO_2 for cobalt ions upon ion implantation at energy of 40 keV is 1.6 atom/ion.

During the DYNA simulation, the near-surface region of the irradiated sample is considered to consist of a set of thin (in our case, ~ 2 nm) parallel-sided layers containing a certain number of atoms of a particular element. The total thickness of the multilayer structure is chosen so that it exceeds the maximum implantation range in a material at a given implantation energy. During the depth profile calculations, the atomic concentration in each layer was determined at each stage after introducing a certain number of accelerated ions and the target

had a new atomic composition for the next implantation step.

Figs. 8 show the simulated depth profiles of Co^+ , Cr^+ , and Cu^+ ions upon implantation in TiO_2 at various doses without and with allowance for the sputtering of the target surface. As is seen from these curves, the concentration profiles change in time dynamically, i.e., as a function of the number of implanted ions in the irradiated material (Fig. 8 curves 1 – 5). At the initial implantation time (i.e., at a low dose), which is not shown in Figs. 3 and 4, the DYNA distribution of implanted ions coincides with the TRIM profile. Longer implantation leads to noticeable sputtering of both target atoms and a certain fraction of implanted atoms from the near-surface layer of the sample. A high-dose implantation is known to cause competing processes that control the depth profile of an impurity [4]. On the one hand, this is surface sputtering; on the other, these are effects related to a change in the atomic composition of the matrix and its density. These effects substantially influence the ion projective range and the character of collisions between implanted ions and atoms in the implanted layer.

As a result, the maximum in the depth profile of the impurity concentration shifts from its position in the TRIM profile toward the irradiated surface. As the ion dose increases, the DYNA distribution shape becomes asymmetric and the position of the concentration maximum shifts toward the irradiated surface, which radically distinguishes this distribution from the TRIM distribution.

The depth profiles and the shift in their maximum with the ion dose are caused by both effects, i.e., a change in the surface elemental composition and surface sputtering. It is difficult to select the contribution of each process. In principle, however, it can imagine a situation where the fraction of sputtered implanted atoms from the surface region is compensated for by introduced ions under certain “equilibrium” implantation conditions; as a result, the depth profile is stabilized and remains unchanged despite a further increase in the implantation dose. In this case, the competing processes are controlled by the rate of introduction of implanted ions and the sputtering coefficient. Thus, the DYNA algorithm computer simulation is in good agreement with experiment and gives realistic depth profiles of implanted ions in irradiated TiO_2 matrices.

Therefore, in this work [52] calculated the depth profiles of chromium and copper ions in TiO_2 with the sputtering coefficient used in the case of cobalt implantation (since their atomic masses are similar) rather than employing expensive depth profile

measurements by Rutherford backscattering. It is obvious that the model examples considered above are certain simplification compared to real implantation conditions; in particular, apart from the calculation parameters noted above, there exist additional competing processes that significantly affect the redistribution of implanted impurities and, correspondingly, their depth profiles. These processes include radiation-assisted and thermal diffusion in implanted materials, impurity segregation, the effect of the crystallographic orientation of the matrix (channeling effect), and so on. Nevertheless, in contrast to the standard TRIM software, our DYNA calculation approach can be used to simulate rather realistic and correct depth profiles of implanted impurities. As a result, we can quantitatively estimate important parameters, such as the implanted-layer thickness, the maximum impurity concentration, the maximum filling with metal, etc., under given ion implantation conditions.

4. CHARACTERISTICS OF IMPLANTED TITANIUM OXIDE

4.1. Photocatalytic properties

Researchers all over the world have been working on various photoinduced processes and supported applications. One important technique for removing industrial waste is the use of light energy (electromagnetic radiation) and material sensitive to this energy. TiO_2 is considered very close to an ideal semiconductor for photocatalysis because of its high stability, low cost and safety toward both humans and the environment.

As was shown in review [1], in 1964, it was published a work [53] on the photocatalytic oxidation of tetralin (1,2,3,4-tetrahydronaphthalene) by a TiO_2 suspension, which was followed by [54] investigating the photocatalytic oxidation of ethylene and propylene in the presence of oxygen adsorbed on TiO_2 . The most important discovery that extensively promoted the field of photocatalysis was the “Honda-Fujishima Effect” first described in 1972 [55]. This well-known chemical phenomenon involves electrolysis of water, which is related to photocatalysis. Photoirradiation of a TiO_2 (rutile) single crystal electrode immersed in an aqueous electrolyte solution induced the evolution of oxygen from the TiO_2 electrode and the evolution of hydrogen from a platinum counterelectrode when an anodic bias was applied to the TiO_2 working electrode. Late TiO_2 has been widely studied with regard to photocatalytic applications such as gas sensors,

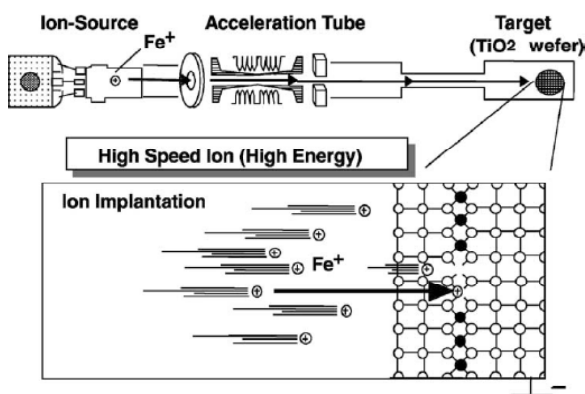


Fig. 9. Systematic diagram of a metal ion Fe^+ -implantation into TiO_2 wafer. Fragment of an image from Ref. [61].

solar cells, and environmental pollutant treatments [56,57].

Unfortunately, conventional titanium oxides such as TiO_2 powdered semiconducting catalysts cannot effectively utilize visible light and make use of only 3-4% of the solar beams that reach the earth, necessitating the use of an ultraviolet light source such as a mercury lamp. Studies into the chemical doping of metal ions into TiO_2 catalyst to explore the possibility of visible light absorption were carried out. However, in these systems, it was found that the various ions doped were present only as impurities enhancing the recombination of the photoformed electrons and holes, and did not enhance reactions with any noticeable effect neither under visible light nor UV light [58].

It is, therefore, necessary to develop a photocatalytic system, which can be applied under visible and/or solar light irradiation. It was shown that the metal ion-implanted TiO_2 photocatalysts with various transition metals such as V and Cr ions absorb visible light and operate effectively under visible or solar light irradiation for the photocatalytic decomposition of NO into N_2 and O_2 as the gas-phase reaction [58-60].

Recently, it was suggested to use Fe^+ ion-implanted TiO_2 photocatalysts which was demonstrated the successful utilization of these catalysts for the photocatalytic degradation of 2-propanol diluted in water under visible light irradiation as a model reaction of the photocatalytic purification of water using solar light [61]. For this purpose the TiO_2 powder with anatase crystalline phase was pressed into a wafer. The Fe^+ ion irradiation of the wafers was carried out using an ion-implanter (Fig. 9) consisting of a metal ion source, mass analyser, and high voltage ion accelerator (150 keV). The metal

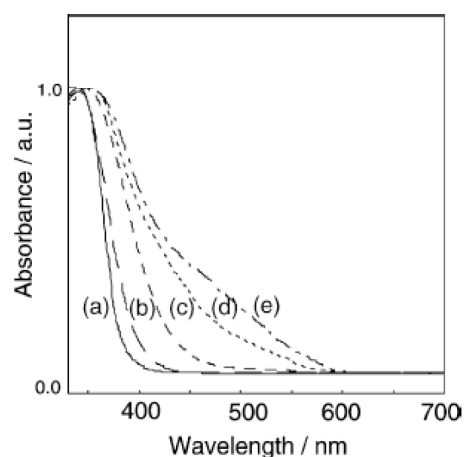


Fig. 10. The diffuse reflectance UV-Vis spectra of TiO_2 (a) and Fe ion-implanted TiO_2 photocatalysts ((b)–(e)). Ion acceleration energy: 150 keV. Amounts of implanted Fe ions ($\cdot 10^{-7}$ mol/g_{cat}): (a) 0, (b) 2.2, (c) 6.6, (d) 13.2, and (e) 22.0. Fragment of an image from Ref. [61].

ions are accelerated in the electronic field and injected to the sample target (TiO_2 wafer) as the ion beam.

As shown in Fig. 10, the absorption band of the TiO_2 implanted with Fe ions with high acceleration energy (150 keV) and calcined in O_2 at 723K after ion-implantation was found to shift to visible light regions, the extent depending on the amount of Fe ions implanted.

The TiO_2 implanted with Fe ions of $(13.2\text{--}22.0)\cdot 10^{-7}$ mol/g_{cat} can absorb the visible light even at around 600 nm. The Fe ions implanted within the bulk of TiO_2 can modify the electronic properties of the TiO_2 surface layer. The ion-implantation with the other transition metal ions such as V, Cr, Mn, Co, Ni, Cu, etc. were found to be also effective to modify the properties of TiO_2 to make a large shift in the absorption band to the visible light region [58-60]. On the other hand, ion-implantation with ions such as Ti, Ar, Na, etc was not effective at all to modify the properties of TiO_2 to make a shift of absorption band to the longer wavelength region.

From the Fourier transforms of EXAFS spectra of the Fe- ion implanted TiO_2 it was detected that Fe ions exist as isolated octahedrally coordinated Fe^{3+} species substituted with lattice Ti^{4+} ions in the lattice of TiO_2 . The same results that the implanted metal ions are substituted with lattice Ti^{4+} ions in the lattice of TiO_2 have been observed by the XAFS analysis with V ion- and Cr ion-implanted TiO_2 [62]. These results suggest that it is important to modify TiO_2 to be able to adsorb visible light and

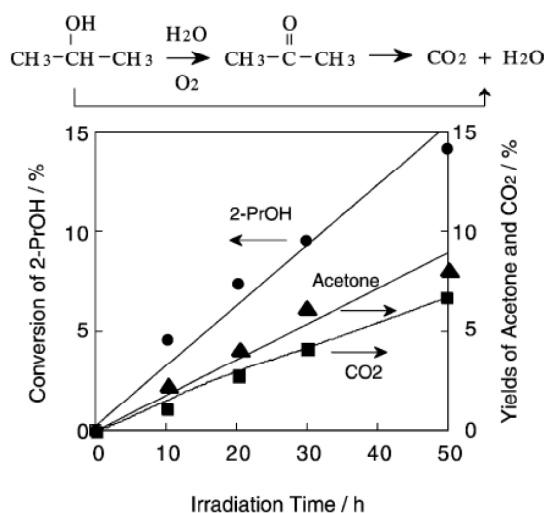


Fig. 11. The reaction time profiles of the photocatalytic oxidative degradation of 2-propanol diluted in water on the Fe ion-implanted TiO_2 photocatalysts under visible light irradiation ($\lambda > 450$ nm). Fragment of an image from Ref. [61].

operate as efficient photocatalyst under visible light irradiation.

The visible light irradiation ($\lambda > 450$ nm) of the Fe ion-implanted TiO_2 in a diluted aqueous solution of 2-propanol under O_2 atmosphere led to the formation of acetone and CO_2 (Fig. 11). After prolonged visible light irradiation acetone is finally decomposed into CO_2 and H_2O . The formation of these products was not detected under dark condition. On the other hand, the unimplanted original TiO_2 photocatalyst did not exhibit any photocatalytic reactivity under visible light irradiation. The presence of the metal ion-implanted TiO_2 as well as visible light irradiation are indispensable for the photocatalytic reaction to take place and the degradation of 2-propanol occurs photocatalytically on the catalyst surface.

4.2. Electrical properties

Ion implantation into TiO_2 revealed that various ions occupy substitutional sites by replacing Ti atoms [64,65]. The replacement of Ti atoms depends in a first approximation on the size mismatch energy of the implanted ions. A summary of all results obtained up till now was given recently [65] where it was shown that atoms with an atomic radii difference of $\Delta r = |r^i - r^{\text{Ti}}|$ up to about 0.02 nm are highly substitutional. With increasing Δr the substitutional component decreased rapidly being zero for “ r values” of 0.04 [66]. The maximum concentration of implanted ions on Ti sites may exceed that obtained

by conventional doping [67]. Thus it is of interest if enhanced electrical doping may be obtained by ion implantation. The electrical conductivity of TiO_2 , σ , increases by many orders of magnitude due to radiation damage [68, 69]. Therefore the influence of disorder and doping on σ can be separated. It was shown that the increase of σ by disorder saturated with fluence at about $1 \text{ } \Omega^{-1}\text{cm}^{-1}$ for Kr and at about $0.3 \text{ } \Omega^{-1}\text{cm}^{-1}$ for Ar implantation. Conductivity values which are larger than these values are generally attributed to the doping action of the implanted species. The next important question concerns the relation between lattice site occupation, possible charge state, and electrical conductivity. Here compensation as well as precipitation effects have to be considered. For Nb implanted into TiO_2 it is assumed that the pentavalent charge state is compensated by defects such as Ti^{3+} , while for Nb doses greater than $1 \times 10^{17} \text{ ion/cm}^2$ electron hopping between Nb and Ti precipitates may occur as charge-transport processes [64]. Implantation of Sn which is substitutional up to concentrations of about 1 at. % leads to an unexpected increase of $5\text{--}30 \text{ } \Omega^{-1}\text{cm}^{-1}$, which is higher than conductivity values of about $1 \text{ } \Omega^{-1}\text{cm}^{-1}$, obtained by conventional doping. This rather high σ value obtained by Sn doping is not well understood as the most probable charge state of Sn is 4^+ , equal to that of Ti in TiO_2 . Therefore it was of interest to study the lattice site occupation and the conductivity of Sb implanted into TiO_2 . For Sb a charge state of 5 is possible and the results may then be compared with those of Nb, which is the most effective dopant found up till now in TiO_2 using ion implantation [64].

As an example it could be mentioned that recently, a conductivity behavior of TiO_2 implanted with Cr ions was also studied [70]. Single crystalline rutile (TiO_2) of [001] orientation was implanted at room temperature with 140 keV Cr^+ ions to doses of the order $10^{17} - 10^{18} \text{ ion/cm}^2$. The electrical resistivity measurements were carried out using a standard four point probe technique in a van der Pauw geometry, for temperatures between 5 and 300K. The reported results refer to constant current measurements taken with $I = 10 \text{ } \mu\text{A}$. Measurements of the electrical conductivity in the as-implanted state can be presented as conductance vs. temperature, $G(T^{-1/4})$ curves (Fig. 12). As seen from this figure no single law can fit the entire curve. However it is possible to separately find best fitting functions for the lower (up to 35K) and higher- T (from 150 up to 300K) domains. For the lower- T domain the best fitting function involves an exponential dependence in $T^{-1/4}$, with $T_0^{-1/4} = 4.54\text{K}^{-1/4}$ ($k_B T_0 = 36$

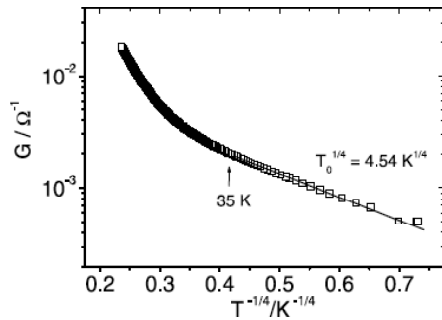


Fig. 12. Conductance–temperature curve $G(T^{-1/4})$, for the as-implanted state. No single law can fit the entire curve. The solid line represents the best fit for lower- T domain. Fragment of an image from Ref. [70].

meV), that describes a variable range hopping of the Mott type between localized defect states. On the other hand, although in the higher- T domain a similar function could also be used, the best fit was obtained by a T^{-1} exponential dependence with activation energy $E_A \approx 30$ meV. This indicates a change to fixed range hopping charge transport at these temperatures.

The values of the electrical conductivity found for the as-implanted state at room temperature fit well in the trend established by previous results in similar rutile single crystals implanted in similar conditions [64,71]. There is an approximate proportionality in the log–log plot of the electrical conductivity and the implanted dose, which indicates some type of doping action of the implanted impurities, which we propose to be of a dual nature: donation of charge carriers by the implanted impurity atoms and the simultaneous introduction of a high density of closely spaced defect states associated with the implantation damage. This would explain the relatively small values of resistance measured at low temperatures (Fig. 12).

Measured values as low as 60Ω for the resistance of the as-implanted state at room temperature correspond to conductivities $\sigma \sim 590 \Omega^{-1} \text{cm}^{-1}$, using $\sigma = G \ln 2 / \rho d$ [64,71] where d is a characteristic length of the conductive layer. Measurement of the Hall constant at RT yielded a value of $R_{\text{Hall}} \approx 2 \times 10^{-9} \text{Vm/TA}$, which corresponds to an effective contribution of approximately 3% of the implanted Cr ions, if it is assumed that either only one type of charge carriers is present or is largely dominant. Although not conclusive the positive sign of R_{Hall} suggests that the majority of charge carriers are positive, consistently with a fraction of the implanted ions being in a Cr^{3+} charge state [72,73].

Thus, for Cr-implanted TiO_2 at room temperature the conductivity changes more than 15 orders of magnitude, from $10^{-13} \Omega^{-1} \text{cm}^{-1}$ to more than $10^{-2} \Omega^{-1} \text{cm}^{-1}$. Immediately after the implantation a highly disorder (amorphous) implanted region is obtained. The electrical conductivity behavior changes from a variable range hopping regime at lower temperatures to fixed range hopping/activated semiconductor transport at temperatures close to room temperature. The activation energies are of ~ 30 to ~ 40 meV in both regimes. It can be attributed that the observed behavior to the presence of a high density of closely spaced localized impurity levels and of impurities that effectively donate charge carriers to populate these levels.

4.3. Optical properties

The additional interest of this review is recent advantages in optical science and technology, such as development of optical random metal-dielectric composites based on metal nanoparticles (MNP) synthesized by ion implantation. Simultaneously with the search for and development of novel technologies intended for nanoparticle synthesis, substantial practical attention has been devoted to designing techniques for controlling the MNP size. This is caused by the fact that the optical properties of MNPs, which are required for various applications, take place up to a certain MNP dimension. In this content, ion implantation nanotechnology allows one to fabricate optical materials with almost any MNP structures, types of metals and their alloys [4-8]; this opens new avenues in engineering nanomaterials with desired properties. Such composites possess fascinating electromagnetic properties, which differ greatly from those of ordinary bulk materials, and they are likely to become ever more important with a miniaturization of optoelectronic and nonlinear optical components.

Nonlinear optics plays a key role in the implementation and development of many photonics techniques for the optical signal processing of information at enhanced speed. Nonlinear materials with implanted MNPs characteristics are interesting for waveguide applications. The nonlinear properties of MNP-containing materials stem from the dependence of their refractive index and nonlinear absorption on incident light intensity. Giant enhancement of nonlinear optical response in a random media with MNPs is often associated with optical excitation of surface plasmon resonances (SPR) that are collective electromagnetic modes and they are strongly dependent on the geometry structure of the

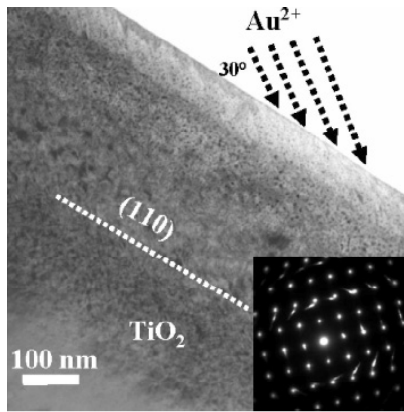


Fig. 13. Bright-field TEM image shows a cross-sectional view of the room temperature as-implanted sample, revealing the general view of the implanted layer thickness. The inset is the selected area electron diffraction pattern. The tail-like feature on the diffraction spots originate from formation of domains in TiO_2 following the Au implantation. Fragment of an image from Ref. [75].

composite medium [74]. Therefore, MNP-containing transparent dielectric and semiconductor materials such as TiO_2 can be effectively applied in novel integrated optoelectronic devices.

MNPs hold great technological promise because of the possibility of engineering with their electronic and optical properties through material design. The noble transition metals of choice are usually gold, silver, or copper, as these metals show SPR modes in the visible or near-infrared spectral range [74]. Therefore, in this review a fabrication of noble MNP in TiO_2 by ion implantation is also considered.

In one of the first work on this subject [75] it was demonstrated that Au nanoparticles could be synthesized in TiO_2 by high-energy ion implantation. 2 MeV Au^{2+} ion implantation at high temperature of substrate were used. Microstructural features of the 300K as-implanted sample are visible in the cross-sectional bright-field TEM image shown in Fig. 13. The dark contrasted dots at a depth of ~ 150 nm from the surface were the Au nanoparticles. The inset of Fig. 13 is the selected area electron diffractions pattern.

The origin of the tail-shaped spots is related to the implantation induced defects formation in the TiO_2 . A close-up view of Fig. 13 is shown in Fig. 14, revealing the Au concentrated regions in Fig. 13. The largest nanoparticles has a dimension of ~ 6 nm.

Recently, authors of work discussed some interesting properties of silver nanoparticles in TiO_2 [76]. For example, Ag-doped TiO_2 films possess

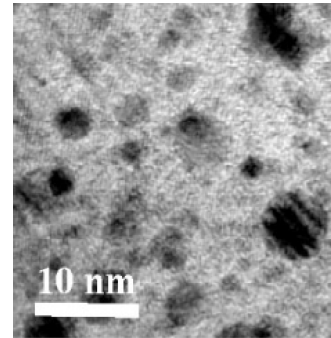


Fig. 14. High magnification image taken from the center of the implanted layer, revealing a general feature of the Au nanoparticles in the room temperature as-implanted specimen. Fragment of an image from Ref. [75].

multi-color photochromism and antibacterial properties [77-79]. It was suggested to create silver nanoparticles in TiO_2 by a metal plasma ion implantation, which was adopted to incorporate trace amounts of Ag ions into the anatase TiO_2 thin films [76]. The metal ion flux, generated by a cathodic arc evaporator, arrives at the substrate surface after being accelerated with a high-voltage grid system. Metal ions with multiple charges interact with the TiO_2 matrix with controlled ion distribution, depth, and dosage. Thus TiO_2 thin film was subjected to metal plasma ion implantation at to incorporate Ag transition metals at ion energy of 40 keV. The implantation doses were $10^{15} - 10^{16}$ ions/cm².

In this study [76], photoluminescence (PL) excited with a He-Cd laser at a wavelength of 325 nm was used to investigate the energy level of TiO_2 . An excitation occurs from the ground singlet

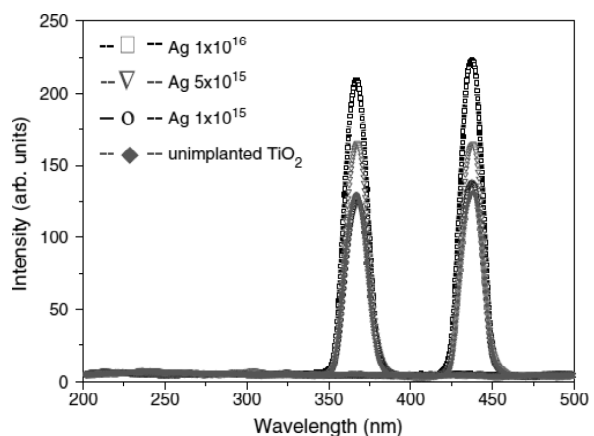


Fig. 15. PL spectra of the virgin TiO_2 and Ag-implanted TiO_2 thin films at various implantation doses. Fragment of an image from Ref. [76].

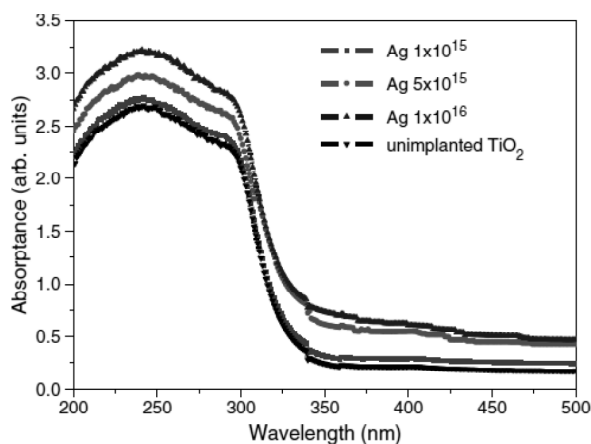


Fig. 16. UV-Vis absorption spectra of the virgin TiO₂ and Ag-implanted TiO₂ thin films at various implantation doses. All the film thicknesses are 370±15 nm. Fragment of an image from Ref. [76].

state to the excited singlet state by the absorption of light coming from the external source. The excited state plays a key role in obtaining phosphorescence. As shown in Fig. 15, the PLs of the pure TiO₂ film were dominated with emission bands of 370 and 440 nm, those were likely assigned to the emission of band gap transition and charge-transfer transition from Ti ions to oxygen anions of TiO₂ [80,81]. The difference of PL spectra between pure TiO₂ and Ag-implanted TiO₂ was caused by the incorporation of Ag ions. The PL emission mainly resulted from the recombination of excited electrons and holes, and the higher PL intensity indicated the increase of recombination rate. The intensities in the PL spectra are quite sensitive to Ag doping. After Ag ion implantation, the PL peak intensities increased even at a low ion dosage of 10¹⁵ ions/cm². The highest emission intensity was obtained at an Ag ion dosage of 10¹⁶ ions/cm². The enhancement of PL intensities was also found in Ag-doped TiO₂ [82]. The increase of PL indicates that the intersystemcrossing of excitation is facilitated as a consequence of the enhancement of the spin orbital coupling by Ag ion implantation.

Fig. 16 shows UV-Vis absorption spectra of the pure TiO₂ and the Ag ion-implanted TiO₂ films deposited on glasses. The pure TiO₂ have an absorption range less than 340 nm. After Ag ion implantation, the absorption rate increased with increasing ion dosage from 10¹⁵ to 10¹⁶ ions/cm². In addition, the absorption range shifted to higher wavelength. The influence of the metal plasma ion implantation on the near-surface microstructure and chemistry resulted mainly from the combined ion mixing and alloying effects. The shift can be as-

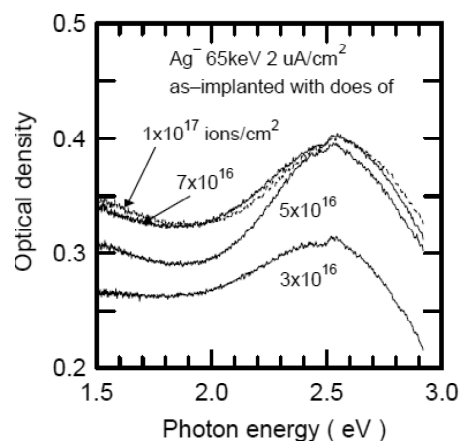


Fig. 17. Optical density spectra of Ag-implanted rutile samples as-implanted with various dose amount. Fragment of an image from Ref. [83].

cribed to the extra Ag impurity energy level which causes to band gap energy decrease and then TiO₂ can be excited at longer wavelength. The evidence for formation of Ag nanoparticles and appearance an optical SPR absorption from them in the work [76] was not demonstrated because of low ion doses applied in this study.

However, as it was show in the work [83,84] silver nanoparticles with the SPR in rutile an sole-gel TiO₂ films can be formed also with low-energy ion implantation but at the higher doses. Silver negative ions were implanted to TiO₂ by using a negative ion implanter with an RF plasma-sputter-type heavy negative ion source. Mass-separated ¹⁰⁷Ag negative ions were implanted at 65 keV. The dose amount was changed from 3·10¹⁶ to 10¹⁷ ions/cm². The ion beam was in size 8 mm in diameter with current density of about 2 μA/cm².

Optical absorption properties measured for Ag-implanted rutile samples are shown in Fig. 17. All Ag-implanted titania samples showed absorption peak near 2.6 eV, while the background optical density in whole range of 1.5 - 3 eV was apparently increased with increase in dose. The background absorption is considered to be due to implantation damage. The absorption peaks for Ag-implanted rutile were different in peak position from the predicted calculated SPR absorption peak. Two main reasons are considered in decrease of refraction index and oxidation of Ag nanoparticles. The increase in background absorption as increasing in dose showed that many defects and voids resulted in the rutile. Therefore, the refraction index of the matrix around nanoparticles might be smaller than original rutile, so that absorption peak of SPR was shifted to position of higher photon energy. When

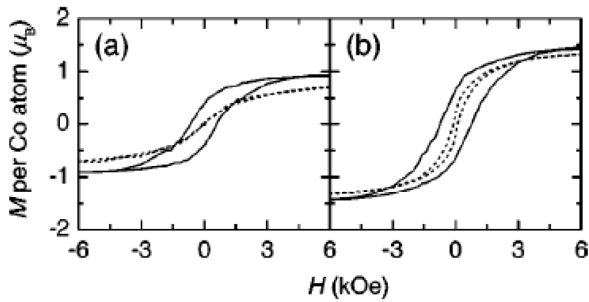


Fig. 18. (a) Magnetization vs magnetic-field curves of the Co-ion-implanted TiO_2 film. The solid and dotted lines are measured at 5 and 300K, respectively. (b) The curves of the film annealed at 600 °C with oxygen pressure of $1.0 \cdot 10^{-6}$ Torr. Fragment of an image from Ref. [92].

the refraction index is $n = 2.0$, the peak position was calculated to be about 2.6 eV. However, this change in refraction index will too large. Another reason of the peak shift of SPR is the formation of alloy or partially oxide nanoparticles.

4.4. Magnetic properties

The continuous attempts to develop next generation devices equipped with multifunctions are now being extended to the search for materials that can combine magnetic responses [85-87]. One example of such efforts is to the quest for a ferromagnetic material system that can inject spin-polarized carriers into semiconductors. Ferromagnetic metals and alloys, such as transition metals, have been found to be inadequate, since spin-polarized carrier injection was found to be difficult due to resistance mismatch. In attempts to overcome such problems, dilute magnetic semiconductors, such as (Ga,Mn)As, (Cd,Mn)GeP₂, (Ga,Mn)N, (Zn,Co)O, and (Ga,Mn)P are claimed to have room temperature ferromagnetism (FM). In spite of extensive efforts in this spintronics area, there has been a great deal of controversy, especially on fundamental issues such as the origins and characteristics of the observed FM.

Oxide semiconductors, in particular, titanium dioxide TiO_2 , doped by iron group transition metal atoms have attracted considerable interest because of the occurrence of room temperature FM [88,89]. These works generated great interest, since it could open possibilities to create new multifunctional oxides that utilize spin polarized carriers. For example, in the work [90] it was reported the magnetic and structural properties of the Co: TiO_2 films grown by oxygen plasma assisted molecular-beam epitaxy and claimed that the FM should be

intrinsic. In the work [91] it was discussed that measured the ion-channeling spectra and temperature-dependent magnetization of Co: TiO_2 films grown by pulsed laser deposition, but suggested that the FM most likely arises from Co nanocluster formation.

Ion implantation can introduce species above the equilibrium solubility limit, provides a new way to investigate diluted magnetic semiconductors. In first pioneer publication on magnetic properties of implanted TiO_2 [92] it was studied the structure and superparamagnetism of anatase epitaxial TiO_2 film implanted with Co^+ ions. Co^+ ions were implanted at a dose of 3 or $5 \cdot 10^{16}$ ion/cm² and energy of 250 keV, which produced incorporation depths of ~ 200 nm and a peak Co-ion concentration of either 3 or 5 at.%. After implantation, the samples were postannealed at a temperature from 300 to 600 °C under O_2 pressure of $1.0 \cdot 10^{-6}$ or $1.0 \cdot 10^{-1}$ Torr.

Magnetic properties of the Co: TiO_2 films were investigated with superconducting quantum interference device. The as-implanted film demonstrated superparamagnetic behaviors. Fig. 18a shows the magnetization versus magnetic-field [$M(H)$] curves of the film, measured at 5K (solid line) and 300K (dotted line). At low temperatures, the film exhibited a hysteretic behavior, indicating that it has FM. However, at room temperature, the FM hysteresis seems to have disappeared.

Room-temperature ferromagnetism in Co-ion implanted rutile was also studied in the work [93]. Single-crystal rutile TiO_2 (110) substrates were purchased and were implanted with 100 keV Co^+ ions at a substrate temperature of 1075K and an

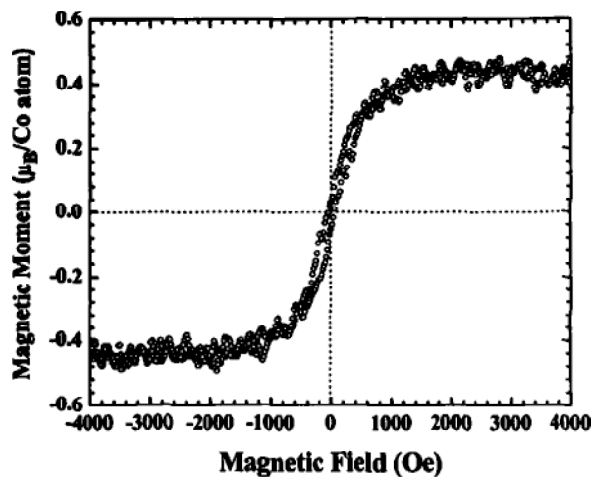


Fig. 19. Room-temperature VSM hysteresis loop for ~ 2 at.% Co-implanted TiO_2 (110) rutile. The substrate temperature was 1075K during implantation. Fragment of an image from Ref. [93].

ion dose of $1.25 \cdot 10^{16}$ ions/cm². Following implantation, the samples were characterized by vibrating sample magnetometry (VSM) to determine the magnetic properties. A typical VSM hysteresis loop taken at room temperature from a Co-implanted TiO₂ (110) rutile sample is shown in Fig. 19. The magnetic field was oriented perpendicular to the sample surface. However, there were no noticeable differences between in-plane and perpendicular magnetization loops. The sample shows clear ferromagnetic behavior with a saturation magnetization of $\sim 0.4 \mu_B/\text{Co atom}$, assuming that all the Co atoms contribute to the magnetization. This value is considerably less than that of pure Co metal ($1.7 \mu_B/\text{Co atom}$), and that found for Co-doped TiO₂ anatase grown by molecular beam epitaxy ($\sim 1.2 \mu_B/\text{Co atom}$) [94]. It is also less than that reported for Co-doped rutile TiO₂ films ($\sim 1 \mu_B/\text{Co atom}$) [95, 96]. The coercive field was found to be ~ 100 Oe and the remanence was $\sim 20\%$.

5. CONCLUSION

In this paper, an overview of the properties, modification by ion implantation and selected applications of TiO₂ as well as its future prospects is presented. Addition of electron donors during ion irradiation can enhance photocatalytic activity by irreversibly reacting with valence band holes to prevent charge recombination. Doping of TiO₂ can inhibit charge recombination and expand its photoresponse to the visible region through the formation of impurity energy levels. Selected applications of implanted TiO₂ for optical and magnetic fields were also observed.

ACKNOWLEDGEMENTS

A.L.S. grateful to the Alexander von Humboldt Foundation, DAAD and DFG in Germany, Austrian Scientific Foundation in the frame of Lisa Meitner Fellowship and the Royal Society in UK for financial support. This work was also supported by the Ministry of Education and Science of the Russian Federation (FTP "Scientific and scientific-pedagogical personnel of the innovative Russia" No. 02.740.11.0779) and the Russian Foundation for Basic Research (¹ 11-02-90420-Ukraine and ¹ 11-02-91341-Germany).

REFERENCES

- [1] S.M. Gupta and M. Tripathi // *Chin. Sci. Bull.* **56** (2011) 1639.

- [2] A. Zaleska // *Recent Patents Eng.* **2** (2008) 157.
- [3] A. Fijushima, T.N. Rao and D.A. Tryk // *J. Photochem. Photobiol. C. Photochem. Rev.* **1** (2000) 1.
- [4] P.T. Townsend, P.J. Chandler and L. Zhang, *Optical effects of ion implantation* (Cambridge Univ. Press: Cambridge, 1994).
- [5] R.F. Haglund Jr., In: *Handbook of optical properties. Vol. II. Optics of small particles, interfaces, and surfaces*, ed. by R.F. Hummel and P. Wismann (CRC Press, London, 1997), p. 198.
- [6] F. Gonella and P. Mazzoldi, In: *Handbook of nanostructured materials and nanotechnology*, ed. by H.S. Nalwa (Academic Press, London, 2000).
- [7] A.L. Stepanov, In: *Metal-Polymer Nanocomposites*, ed. by L. Nicolais and G. Carotenuto (John Wiley & Sons Publ, London, 2004), p. 241.
- [8] A. L. Stepanov, *Ion-synthesis of metal nanoparticles and their optical properties* (Nova Sci. Publ., New York, 2011).
- [9] M. Anpo // *Pure Appl. Chem.* **72** (2000) 1787.
- [10] M. Fuerte, A.J. Maria, A. Martinez-Arias, M. Fernandez-Garcie, J.C. Conesa and J. Soria // *Chem. Commun.* **24** (2001) 2718.
- [11] H. Yamashita, M. Harada, J. Misaka, M. Takeuchi, Y. Ichihashi, F. Goto, M. Ishida, T. Sasaki and M. Anpo // *J. Synchrotron Rad.* **8** (2001) 569.
- [12] T. Ihara, M. Miyoshi, M. Ando, S. Sugihara and Y. Iriyama // *J. Mater. Sci.* **36** (2001) 4201.
- [13] K. Takeuchi, I. Nakamura, O. Matsumoto, S. Sugihara, M. Ando and T. Ihara // *Chem. Lett.* **29** (2000) 1354.
- [14] T. Ohno, T. Mitsui and M. Matsumura // *Chem. Lett.* **32** (2003) 364.
- [15] Y. Liu, X. Chen, J. Li and C. Burda // *Chemosphere* **61** (2005) 11.
- [16] J.C. Yu, L. Zhang, Z. Zheng and J. Zhao // *Chem. Mater.* **15** (2003) 2280.
- [17] O. Carp, C.L. Huisman and A. Reller // *Prog. Solid Stat Chem.* **32** (2004) 33.
- [18] D.T. Cromer and K.J. Herrington // *Am. Chem. Soc.* **77** (1955) 4708.
- [19] V.W.H. Baur // *Acta Cryst.* **14** (1961) 214.
- [20] S. Mo and W. Ching // *Phys. Rev. B* **51** (1995) 13023.
- [21] P.Y. Simons and F. Dacheille // *Acta Cryst.* **23** (1967) 334.

- [22] M. Lacroche, L. Brohan, R. Marchand and M.J. Tournoux // *Solid Stat Chem.* **81** (1989) 78.
- [23] M. Chen and S.S. Mao // *Chem. Rev.* **107** (2007) 2891.
- [24] T.L. Thompson and J.T. Yates Jr. // *Chem. Rev.* **196** (2006) 4428.
- [25] U. Diebold // *Sur. Sci. Rep.* **48** (2003) 53.
- [26] A. Norotsky, J.C. Jamieson and O.J. Kleppa // *Science* **158** (1967) 338.
- [27] Q. Zhang, L. Gao and J. Guo // *Appl. Catal. B* **26** (2000) 207.
- [28] A. Sclafani, L. Palmisano and M. Schiavello // *J. Phys. Chem.* **94** (1990) 829.
- [29] J. Muscat, V. Swamy and T. Harrison // *Phys. Rev. B* **65** (2002) 1.
- [30] K. Tanaka, M.F.V. Capule and T. Hisanaga // *Chem. Phys. Lett.* **187** (1991) 73.
- [31] A. Selloni // *Nature Mater.* **7** (2008) 613.
- [32] H.G. Yang, C.H. Sun, S.Z. Qiao, J. Zhou, S.C. Smith, H.M. Cheng and G.Q. Lu // *Nature* **453** (2008) 638.
- [33] W. Wunderlich, T. Oekermann and L. Miao // *J. Ceram. Process Res.* **5** (2004) 343.
- [34] A.T. Paxton and L. Thien-Nga // *Phys. Rev. B* **57** (1998) 1579.
- [35] S. Banerjee, J. Gopal, P. Muraleedhran, A.K. Tyaigi and A. Raj // *Current Sci.* **90** (2006) 1378.
- [36] M. Chen, G. Li and M. E. Graham // *J. Mol. A Chem.* **275** (2007) 30.
- [37] M.R. Hoffman, S.T. Martin, W. Choi and D.W. Bahnemann // *Chem. Rev.* **95** (1995) 69.
- [38] A. Fijushima, T.N. Rao and D.A. Tryk // *J. Photochem. Photobiol. C. Photochem. Rev.* **1** (2000) 1.
- [39] R. Asahi, T. Morikawa, T. Ohwaki, K. Aoki and Y. Taga // *Science* **293** (2001) 269.
- [40] H. Ire, Y. Watanabe and K. Hashimoto // *J. Phys. Chem. B* **107** (2003) 5483.
- [41] T. Ihara, M. Miyoshi, Y. Triyama, O. Marsumato and S. Sugihara // *Appl. Catal. B* **42** (2003) 403.
- [42] Z. Zhao and Q. Liu // *J. Phys. D: Appl. Phys.* **41** (2008) 1.
- [43] A.L. Stepanov, In: *Silver nanoparticles*, ed. by D.D. Perez (In-Tech, Vucovar, 2010), p. 93.
- [44] S. Deying, Y. Saito and S. Suganomata // *Jpn. J. Appl. Phys.* **33** (1994) L96.
- [45] A.L. Stepanov, S.N. Abdullin, R.I. Khaibullin, V.F. Valeev, Yu.N. Osin, V.V. Bazarov and I.B. Khaibullin // *Mat. Res. Soc. Proc.* **392** (1995) 267.
- [46] A.L. Stepanov, D.E. Hole and P.D. Townsend // *Nucl. Instr. Meth. Phys. Res.* **129** (1999) 89.
- [47] J.F. Ziegler, J.P. Biersak and U. Littmark, *The stopping and range of ions in solids* (Pergamon, New York, 1996).
- [48] V.M. Konoplev // *Radiat. Eff. Lett.* **87** (1986) 207.
- [49] V.M. Konoplev // *Nucl. Instr. Meth. Phys. Res.* **43** (1989) 159.
- [50] V.M. Konoplev, M. Vicanek and A. Gras-Marti // *Nucl. Instr. Meth. Phys. Res.* **67** (1992) 574.
- [51] A.L. Stepanov, V.A. Zhikharev, D.E. Hole, P.D. Townsend and I.B. Khaibullin // *Nucl. Instr. Meth. Phys. Res. B* **166-167** (2000) 26.
- [52] A.L. Stepanov, V.F. Valeev, V.I. Nuzhdin, R.I. Khaibullin, Yu.N. Osin and I.A. Faizrahmanov // *Tech. Phys.* **53** (2008) 1070.
- [53] S. Kato and F. Masuo // *Kogyo Kagaku Zasshi* **67** (1964) 42.
- [54] S. McLintock and M. Ritchie // *Trans. Faraday Soc.* **61** (1965) 1007.
- [55] A. Fujishima and K. Honda // *Nature* **238** (1972) 37.
- [56] *Photocatalytic purification and treatment of water and air*, ed. by D.F. Ollis and H. Al-Ekabi (Elsevier, Amsterdam, 1993).
- [57] *Photochemical conversion and storage of solar energy*, ed. by E. Pelizzetti and M. Schiavello (Kluwer Acad. Publ., New York, 1991).
- [58] M. Anpo, Y. Ichihashi, M. Takeuchi and H. Yamashita // *Res. Chem. Intermed.* **24** (1998) 143.
- [59] M. Anpo // *Catal. Surv. Jpn.* **1** (1997) 169.
- [60] M. Anpo, Y. Ichihashi, M. Takeuchi and H. Yamashita // *Stud. Surf. Sci. Catal.* **121** (1999) 305.
- [61] M. Anpo and M. Che // *Adv. Catal.* **44** (1999) 119.
- [62] H. Yamashita, M. Harada, J. Misaka, M. Takeuchi, B. Neppolian and M. Anpo // *Catal. Today* **84** (2003) 191.
- [63] H. Yamashita, M. Honda, M. Harada, Y. Ichihashi, M. Anpo, T. Hirao, N. Itoh and N. Iwamoto // *J. Chem. Phys. B* **102** (1998) 10707.
- [64] S.M.M. Ramos, B. Canut, R. Brenier, I. Gea, L. Romana, M. Brunel and P. Thevenard // *Nucl. Instr. Meth. Phys. Res. B* **80-81** (1993) 1123.

- [65] R. Fromknecht, I. Kubeis and O. Meyer // *Nucl. Instr. Meth. Phys. Res. B* **116** (1996) 109.
- [66] R. Fromknecht and O. Meyer // *Mater. Chem. Phys.* **45** (1996) 50.
- [67] J.W. DeFord and O.W. Johnson // *J. Appl. Phys.* **54** (1983) 889.
- [68] T.E. Parker and R. Kelly // *J. Phys. Chem. Solids* **36** (1975) 377386.
- [69] I. Kubeis, R. Fromknecht and O. Meyer // *Phys. Rev. B* **55** (1997) 136.
- [70] R.C. da Silva, E. Alves and M.M. Cruz // *Nucl. Instr. Meth. Phys. Res. B* **191** (2002) 158.
- [71] R. Fromknecht, R. Auer, I. Kubeis and O. Meyer // *Nucl. Instr. Meth. Phys. Res. B* **120** (1996) 252.
- [72] K. Mizushima, M. Tanaka and S. Iida // *J. Phys. Soc. Jap.* **32** (1972) 1519.
- [73] K. Mizushima, M. Tanaka, A. Asai, S. Iida and J.B. Goodenough // *J. Phys. Chem. Solids* **40** (1979) 1129.
- [74] U. Kreibig and M. Vollmer, *Optical properties of metal clusters* (Springer, Berlin, 1995).
- [75] C.M. Wang, Y. Zhang, V. Shutthanandan, S. Thevuthasan and G. Duscher // *J. Appl. Phys.* **95** (2004) 8185.
- [76] Y.-Y. Chang, Y.-N. Shieh and H.-Y. Kao // *Thin Solid Films* **519** (2011) 6835.
- [77] Y. Ohko, T. Tatsuma, T. Fujii, K. Naoi, C. Niwa, Y. Kubota and A. Fujishima // *Nat. Mater.* **2** (2003) 29.
- [78] M.J. Uddin, F. Cesano, S. Bertarione, F. Bonini, S. Bordiga, D. Scarano and A.J. Zecchina // *Photochem. Photobiol. A* **196** (2008) 165.
- [79] Y. Liu, X. Wang, F. Yang and X. Yang // *Microporous Mesoporous Mater.* **114** (2008) 431.
- [80] H.Y. Chuang and D.H. Chen // *Nanotechnology* **20** (2009) 195705-1.
- [81] F.B. Li and X.Z. Li // *Chemosphere* **48** (2002) 1103.
- [82] J.C. Yu, H.G. Yu, B. Cheng, X.J. Zhao, J.C. Yu and W.K. Ho // *J. Phys. Chem. B* **107** (2003) 13871.
- [83] H. Tsuji, H. Sugahara, Y. Gotoh and J. Ishikawa // *IEEE* **12** (2002) 705.
- [84] H. Tsuji, N. Sakai, H. Sugahara, Y. Gotoh and J. Ishikawa // *Nucl. Instr. Meth. Phys. Res. B* **237** (2005) 433.
- [85] H. Ohno // *Science* **281** (1998) 951.
- [86] A. Kaminski and S. Das Sarma // *Phys. Rev. Lett.* **88** (2002) 247202.
- [87] M. Berciu and R.N. Bhatt // *Phys. Rev. B* **69** (2004) 45202-1.
- [88] Y. Matsumoto, M. Murakami, T. Shono, T. Hasegawa, T. Fukumura, M. Kawasaki, P. Ahmet, T. Chikyow, S. Kashiwara and H. Koinuma // *Science* **291** (2001) 854.
- [89] D.H. Kim, J.S. Yang, K.W. Lee, S.D. Bu, D.-W. Kim, T.W. Noh, S.-J. Oh, Y.-W. Kim and J.-S. Chung // *J. Appl. Phys.* **93** (2003) 6125.
- [90] S.A. Chambers, S. Thevuthasan, R.F.C. Farrow, R.F. Marks, J.U. Thiel, L. Folks, M.G. Samat, A.J. Kellock, N. Ruzycski, D.L. Ederer and U. Diebold // *Appl. Phys. Lett.* **79** (2001) 3467.
- [91] D.H. Kim, J.S. Yang, K.W. Lee, S.D. Bu, T.W. Noh, S.-J. Oh, Y.-W. Kim, J.-S. Chung, H. Tanaka, H.Y. Lee and T. Kawai // *Appl. Phys. Lett.* **81** (2002) 2421.
- [92] D.H. Kim, J.S. Yang, D.-W. Kim, T.W. Noh, S.D. Bu, Y.-W. Kim, Y.D. Park, S.J. Pearton, Y. Jo and J.-G. Park // *Appl. Phys. Lett.* **83** (2003) 4574.
- [93] V. Shutthanandan, S. Thevuthasan, S.M. Heald, T. Droubay, M.H. Engelhard, T.C. Kaspar, D.E. McCready, L. Saraf, S.A. Chambers, B.S. Mun, N. Hamdan, P. Nachimuthu, B. Taylor, R.P. Sears and B. Sinkovic // *Appl. Phys. Lett.* **84** (2004) 4466.
- [94] S. A. Chambers and R.F.C. Farrow // *MRS Bull.* **28** (2003) 729.
- [95] Y. Matsumoto, R. Takahashi, M. Murakami, T. Koida, X.-J. Fan, T. Hasegawa, T. Fukumura, M. Kawasaki, S.-Y. Koshiwara and H. Koinuma // *Jpn. J. Appl. Phys. Part-2* **91** (2001) L1204.
- [96] W.K. Park, R.J. Ortega-Hertogs, J. Moodera, A. Punnoose and M.S. Seehra // *J. Appl. Phys.* **91** (2002) 8093.